

Improved limit on neutrinoless double beta decay of ^{100}Mo from AMoRE-I

A. Agrawal , V.V. Alenkov , P. Aryal , J. Beyer , B. Bhandari , R.S. Boiko , K. Boonin , O. Buzanov , C.R. Byeon , N. Chanthima , M.K. Cheoun , J.S. Choe , Seonho Choi , S. Choudhury , J.S. Chung , F.A. Danevich , M. Djamel , D. Drung , C. Enss , A. Fleischmann , A.M. Gangapshv , L. Gastaldo , Y.M. Gavriluk , A.M. Gezhav , O. Gileva , V.D. Grigorieva , V.I. Gurentsov , C. Ha , D.H. Ha , E.J. Ha , D.H. Hwang , E.J. Jeon , J.A. Jeon , H.S. Jo , J. Kaewkhao , C.S. Kang , W.G. Kang , V. V. Kazalov , S. Kempf , A. Khan , S. Khan , D.Y. Kim , G.W. Kim , H.B. Kim , Ho-Jong Kim , H.J. Kim , H.L. Kim , H.S. Kim , M.B. Kim , S.C. Kim , S.K. Kim , S.R. Kim , W.T. Kim , Y.D. Kim , Y.H. Kim , K. Kirdsiri , Y.J. Ko , V.V. Kobychv , V. Kornoukhov , V.V. Kuzminov , D.H. Kwon , C.H. Lee , DongYeup Lee , E.K. Lee , H.J. Lee , H.S. Lee , J. Lee , J.Y. Lee , K.B. Lee , M.H. Lee , M.K. Lee , S.W. Lee , Y.C. Lee , D.S. Leonard , H.S. Lim , B. Mailyan , E.P. Makarov , P. Nyanda , Y. Oh ,* S.L. Olsen , S.I. Panasenko , H.K. Park , H.S. Park , K.S. Park , S.Y. Park , O.G. Polischuk , H. Prihtiadi , S. Ra , S.S. Ratkevich , G. Rooh , M.B. Sari , J. Seo , K.M. Seo , B. Sharma , K.A. Shin , V.N. Shlegel , K. Siyeon , J. So , N.V. Sokur , J.K. Son , J.W. Song , N. Srisittipokakun , V.I. Tretyak , R. Wirawan , K.R. Woo , H.J. Yeon , Y.S. Yoon , and Q. Yue

(AMoRE Collaboration)

(Dated: July 9, 2024)

AMoRE searches for the signature of neutrinoless double beta decay of ^{100}Mo with a 100 kg sample of enriched ^{100}Mo . Scintillating molybdate crystals coupled with a metallic magnetic calorimeter operate at milli-Kelvin temperatures to measure the energy of electrons emitted in the decay. As a demonstration of the full-scale AMoRE, we conducted AMoRE-I, a pre-experiment with 18 molybdate crystals, at the Yangyang Underground Laboratory for over two years. The exposure was 8.02 kg-year (or 3.89 kg ^{100}Mo -year) and the total background rate near the Q-value was 0.025 ± 0.002 counts/keV/kg/year. We observed no indication of $0\nu\beta\beta$ decay and report a new lower limit of the half-life of ^{100}Mo $0\nu\beta\beta$ decay as $T_{1/2}^{0\nu} > 3.0 \times 10^{24}$ years at 90% confidence level. The effective Majorana mass limit range is $m_{\beta\beta} < (210\text{--}610)$ meV using nuclear matrix elements estimated in the framework of different models, including the recent shell model calculations.

Experiments with solar and atmospheric neutrinos [1, 2] have found that neutrinos are massive. Various oscillation experiments [3–6] have measured the three mixing angles and two mass differences. Although the absolute masses of neutrinos have not yet been measured, we know they are very small, less than 1 eV/ c^2 based on measurements of the endpoint of the tritium beta-decay energy spectrum and from cosmological observations [7, 8].

The small neutrino masses and the absence of right-handed neutrinos in the Standard Model motivated the introduction of Majorana masses for neutrinos, as opposed to charged leptons that have Dirac masses. Small Majorana neutrino mass can be generated via the seesaw mechanism in which the masses of active neutrinos are suppressed by heavy right-handed sterile neutrinos [9], and the mass terms violate lepton number conservation [10].

The currently well-established method for determining if neutrinos are Majorana fermions is to search for neutrinoless double beta ($0\nu\beta\beta$) decay of nuclei [11]. Regardless of the underlying mechanism, the observation of $0\nu\beta\beta$ decay would prove that lepton number is violated [12], which is necessary for the seesaw mechanism and leptogenesis [13]. The amplitude of $0\nu\beta\beta$ decay is proportional to the effective Majorana mass, defined

by the charged-current couplings of Majorana neutrinos. The main challenge in $0\nu\beta\beta$ decay experiments is achieving the sensitivity to reach the true effective Majorana mass. A $0\nu\beta\beta$ decay experiment requires monitoring a large mass of isotopes with a detector having an ultra-low background and a high energy resolution. In spite of more than seventy years of experimental efforts [14], no signal for $0\nu\beta\beta$ decay has been observed. The best half-life limit has been established by KamLAND-Zen for ^{136}Xe with $T_{1/2}^{0\nu} > 2.3 \times 10^{26}$ years, limiting the effective Majorana mass to $m_{\beta\beta} < (36\text{--}156)$ meV [15]. For other isotopes, the limits of $T_{1/2}^{0\nu}$ ($m_{\beta\beta}$) are: 3.3×10^{25} years (90–305 meV) for ^{130}Te by CUORE using cryogenic techniques [16], 1.8×10^{26} years (79–180 meV) for ^{76}Ge by GERDA using high purity germanium detectors [17], and 1.8×10^{24} years (280–490 meV) for ^{100}Mo by CUPID-Mo using cryogenic scintillating crystal detectors [18, 19].

AMoRE searches for the $0\nu\beta\beta$ decays using molybdate-based crystal detectors operating at milli-Kelvin (mK) temperatures [20, 21], similar to CUPID-Mo. AMoRE aims to achieve zero background, defined as less than one count in the region of interest (ROI) near $Q_{\beta\beta} = 3034.4$ keV for the five-year duration of the experiment with a detector array of about 100 kg of ^{100}Mo isotope.

The AMoRE project is progressing in three phases. The first two phases, AMoRE-Pilot and AMoRE-I, were completed at the 700-meter-deep Yangyang Underground Laboratory (Y2L). AMoRE-II will run at the newly built Yemilab for five years. We have reported a half-life limit of $T_{1/2}^{0\nu} = 3.0 \times 10^{23}$ years at a 90% confidence level (CL) using six $^{48\text{depl}}\text{Ca}^{100}\text{MoO}_4$ crystals in the AMoRE-Pilot run [22–24]. To confirm the performance and long-term stability of the detection system and determine the low background level that is achievable with the existing underground setup, we operated AMoRE-I from 2019 to 2023. The AMoRE-I detector array consists of eighteen crystals with a total mass of 6.2 kg, including 3.0 kg of ^{100}Mo . This report describes the experimental setup, data analysis, and the results on a new half-life limit of ^{100}Mo .

AMoRE-I was carried out in the same cryostat and shielding arrangement that was used for AMoRE-Pilot [22–25], but with a larger number of detectors. We made a few modifications to the detector modules and shielding enhancements. The AMoRE-I system used a two-stage temperature control system to maintain the detector tower at a constant temperature [26]. The datasets used for this report were taken at a temperature of 12 mK.

The AMoRE-I detector array comprised five $\text{Li}_2^{100}\text{MoO}_4$ (LMO) crystals, and thirteen $^{48\text{depl}}\text{Ca}^{100}\text{MoO}_4$ (CMO) crystals, six of which were inherited from AMoRE-Pilot. The molybdenum isotopes in the crystals were enriched with ^{100}Mo at $95.7 \pm 0.2\%$. Each detector module consisted of a crystal surrounded by a Vikuiti reflector film, an MMC sensor connected to the crystal, and a light detector made of an absorber with an MMC sensor. The mass-spring vibration damping system [27] was removed to accommodate the increased number of detector modules. The stainless steel screws in the detector modules were replaced with copper and brass for lower radioactive contamination. Additionally, Si wafers with SiO_2 antireflection coating were used for the light absorber instead of Ge wafers [28]. One flat surface of the LMO crystal, upon which the gold phonon collector was evaporated, was ground with 1500-grit SiC sandpaper to enhance the gold film bond at the interface. Each crystal had a stabilization heater attached to the flat surface to measure and correct the gain drift of the heat signal [29], primarily due to temperature fluctuations. Pulses of fixed current and duration were injected through the heater every 10 seconds. Detailed descriptions of the detector module can be found in [26, 30].

An additional 5 cm of lead was added outside of the cryostat vacuum chamber to further reduce high-energy environmental γ 's. Initially, aluminum plates were used to support the lead bricks, but these plates were found to be highly contaminated by ^{228}Ra and were removed in

May 2021. Ten additional muon counters made of plastic-scintillator panels were installed to extend the solid-angle coverage for the detector array.

Heat and light signals from the SQUID electronics were continuously digitized without an event trigger and stored using flash analog-to-digital converter modules with an 18-bit resolution for a 10-volt peak-to-peak dynamic range at a 100 kHz sampling frequency. Data acquisition (DAQ) with the full eighteen-crystal detector array started in December 2020 and ended in April 2023, with a 93% live time. About 78% of the DAQ live time was dedicated to physics measurement, while calibration and other commissioning data took up the remaining time. For calibration runs, which took place every 4-8 weeks, depending on the detector's stability, welding rods containing small amounts of thorium were placed between the outer vacuum chamber and the external lead shielding.

To suppress noise, the heat signal of each detector was processed using a Butterworth bandpass filter for the off-line analysis. For most detectors, the trigger thresholds were set below 100 keV. Two modules that suffered from a significant vibration or electric noise had higher thresholds. The amplitudes of the heat and light signals were determined by fitting template waveforms to the data using a least-squares fit [31]. The fit was applied to the filtered waveforms and the bandwidths of the Butterworth filters were optimized to provide the highest energy resolutions. A template signal was constructed by averaging raw signals from 2.615 MeV γ events that were accumulated during calibration runs. The fit result easily distinguishes non-physical events such as SQUID jumps or reset signals. The rise and fall times were derived from the raw signals, defined as the time elapsed between specific points on the pulse. Unlike the AMoRE-pilot analysis, which used the time difference between the 10 and 90% levels of the signal, this analysis defined rise time (RT) variably for each detector, optimizing the pulse shape discrimination (PSD) power. One LMO detector had a noisy light signal, making it impossible to calculate the light signal amplitude accurately. Data from this detector were excluded from the analysis because of the limited PSD power. Examples of the RT versus signal amplitudes for a CMO and an LMO detector are shown in Figure 1.

The detector response change over time, mainly caused by temperature, variations, influenced the pulse amplitudes and shapes of both physics and heater signals. Correlations between the heater signal's RT and the amplitude of 2.615 MeV γ events were determined with calibration data and used for drift correction in the corresponding dataset. A dataset consists of a calibration run followed by physics runs before the next calibration.

The β/γ energy scale was initially calibrated using four prominent γ peaks at 511.0 keV, 583.2 keV, 911.2 keV, and 2614.5 keV in the spectrum taken with the source

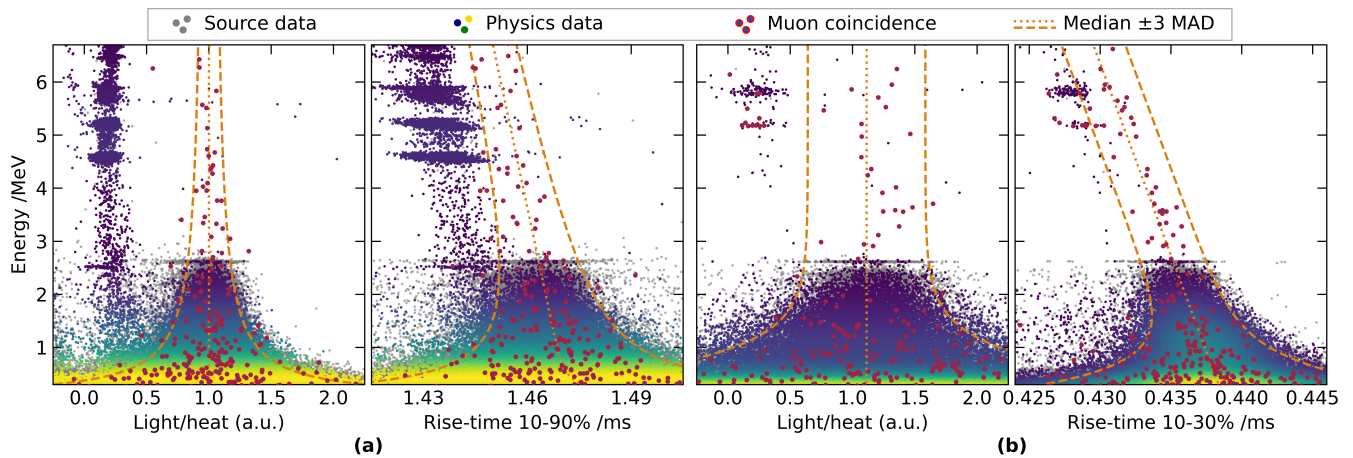


FIG. 1. Particle discrimination parameters: light-to-heat amplitude ratios (L/H) and the raw heat signals' rise times (RT) of (a) CMO06 and (b) LMO02 detectors. Dots with blue-yellow color gradients denote physics data, overlaid on the source data denoted as gray dots. Events in both 3-MAD bands for L/H and RT denoted as dashed-orange curves were selected as β/γ events. Events in the muon veto window are indicated by red circles. Some α -like events with muon coincidence at the electron equivalent energy slightly above 5 MeV in the LMO data are caused by the capture of muon-induced neutrons on the lithium-6 nuclei: ${}^6\text{Li}(n, \alpha)t$.

for each dataset. As in the previous analysis, signal amplitudes for each detector were all well described as a quadratic function of true energy values, without a constant term [22, 32]. Secondary energy calibration was performed using another quadratic function with a constant term, including more γ peaks from the combined calibration data.

Due to non-uniform, position-dependent detector responses, peaks in most detectors' energy spectra were asymmetric, showing tails on both the lower and upper sides. Among various peak-fitting functions, the Bukin function [33] was found to be well-suited for all of the peaks in the calibration spectrum. The spectra around the 2.615 MeV peak in the calibration data for a CMO and an LMO detector are shown in Figure 2. Shape parameters that were determined from fitting below 2.615 MeV were extrapolated to $Q_{\beta\beta}$ to estimate the $0\nu\beta\beta$ signal shape. The squares of energy resolutions (h^2) were well-fitted to a quadratic function of energy. Other shape parameters for asymmetry (ξ), left-tail (ρ_L), and right-tail (ρ_R) varied slowly with energy, and their uncertainties were extrapolated using a linear function or were left constant, depending on each detector's characteristics.

The $0\nu\beta\beta$ event-selection criteria for background reduction were divided into two categories. The first category was particle identification to remove the continuous α background around the ROI due to radioactive contamination on the crystal surface or surrounding materials. Two parameters were adopted for each detector: PSD using RT of the heat signal, and the light-to-heat amplitude ratio (L/H), which leverages the differences in scintillation quenching for α and β/γ particles. Figure 1 shows the RT and L/H versus energy for the calibration runs,

background runs, and events that were coincident with muons for one CMO and one LMO detectors. Here, the α events are clustered at higher energies and at smaller RT and L/H values, while most of the β/γ events without muon coincidence lie below 2.6 MeV.

The median-absolute-deviation (MAD) values were determined using source data at the energy range of 465-2665 keV and fitted using a function of energy. Events within the 3 MAD bands for RT and L/H, denoted as the dashed-orange curves in Figure 1 were selected as β/γ events. The selection efficiencies at the calibration γ -peak energies were determined by comparing the event counts at each peak before and after the selection using the Bukin function on top of a simple exponential or linear background to extract the peak counts from the resulting spectra. These β/γ selection efficiencies, when extrapolated to $Q_{\beta\beta}$, varied among detectors and ranged between 80 and 95% with uncertainties around the 1% level. Generally, CMO detectors showed a much better discrimination power than LMO, for both RT and L/H parameters, due to the higher light yield and the correlation of light yield with the pulse shape [34, 35]. The alpha backgrounds for the six CMO detectors used in AMoRE-Pilot were reported in [23]. The activities of ${}^{226}\text{Ra}$ (${}^{228}\text{Th}$) for the AMoRE-I data set were determined by analysis of $\alpha - \alpha$ coincident events from the sequential decay of ${}^{222}\text{Rn}$ and ${}^{218}\text{Po}$ (${}^{224}\text{Ra}$ and ${}^{220}\text{Rn}$). These were 5–59 $\mu\text{Bq/kg}$ (1–13 $\mu\text{Bq/kg}$) in the CMO detectors, except for one highly contaminated CMO crystal, and 1–2 $\mu\text{Bq/kg}$ for both ${}^{226}\text{Ra}$ and ${}^{228}\text{Th}$ in the LMO detectors. Detailed background modeling of AMoRE-I is in progress.

The second event-selection category involved a series

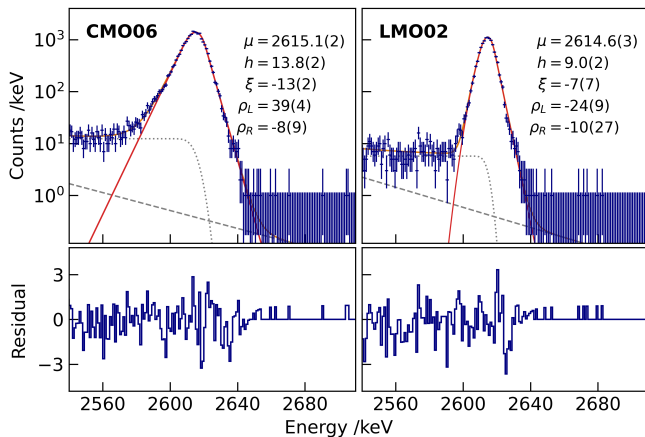


FIG. 2. Part of the energy spectrum measured with the Th-containing sources (blue points with error bars) around 2.615 MeV γ peaks for a CMO crystal (left) and an LMO crystal (right) are shown at the top. The fit function (solid-orange curve) consists of an exponential (dashed-gray curve) plus a smeared-step (dotted-gray curve) background component and a peak signal component that is represented by a Bukin function (solid-red curve). For the Bukin function, the peak location (μ) and the full-width-at-half-maximum energy resolution (h) are given in keV units, and the asymmetry (ξ), left-tail (ρ_L), and right-tail (ρ_R) parameters are in percent. The bottom panels show the fit residuals for the data bins with positive counts as: $([\text{data}] - [\text{fit}])/\sqrt{[\text{data}]}$.

of anti-coincidence cuts. First, events occurring within 10 ms after a muon candidate event were rejected. About ten thousand muon candidate events were registered daily, resulting in an inefficiency of only 0.1% with negligible uncertainty. Secondly, we imposed a single-hit requirement that the signal candidate is the only hit that occurred within a 2 ms time window. Since the trigger rate of the background runs was typically about 1 Hz, the efficiency of this single-hit requirement was about 99.8%. The final anti-coincidence condition, called α -tagging, targeted one of the major backgrounds in the ROI from the beta decay of ^{208}Tl with $Q \sim 4.998$ MeV. These background events follow an α event emitted in ^{212}Bi decay to ^{208}Tl . Since the half-life of ^{208}Tl is 3.053 minutes and the energy released in the α decay of ^{212}Bi is 6.207 MeV, all events within 20 minutes after an α event in the same crystal with 6.2 ± 0.1 MeV energy were rejected. Two detectors with exceptionally high α event rates had a narrower α energy window of 0.04 MeV [23]. The efficiency of this α -veto was about 98% on average: 78% for the most α -contaminated CMO and higher than 99% for LMOs. The cut efficiencies are summarized in Table I.

Figure 3 shows the resulting background energy spectra accumulated for 8.02 kg-year (or 3.89 kg^{100}Mo -year) exposure, following step-by-step selections, overlaid with the calibration spectrum. The first dataset taken with the aluminum support plate, shown as the dark blue

TABLE I. Efficiencies of the selection cuts utilized to suppress background in the vicinity of the expected $0\nu\beta\beta$ peak, and the typical systematic uncertainties. The efficiencies averaged over all the detectors are given in parentheses. The $0\nu\beta\beta$ containment efficiency is calculated using the DECAY-0 event generator [37] and the GEANT4-based detector simulation [36].

Parameters/selection	Efficiency (%)	Uncertainty (%)
Particle identification		
PSD \times L/H (3 MAD)	78.8-95.4 (89.9)	1.6
Anti-coincidences		
Multiplicity ($\mathcal{M} = 1$)	99.8	<0.1
Muon veto (10 ms)	99.9	<0.1
^{212}Bi α veto (20 min)	77.6-99.8 (97.8)	0.6
$0\nu\beta\beta$ containment	78.4-82.4 (81.1)	1.0
Total detection efficiency	49.1-76.1 (70.9)	1.6

shaded area, represents about 14% of total exposure but contains about 20% of the events in the energy range below 2.7 MeV, including about 60% of 2.615 MeV γ events. Despite this, the background due to the contaminated aluminum plate is mainly confined to energies below 2.7 MeV, so these data were included in the $0\nu\beta\beta$ analysis. As shown in the previous studies [22], the relationship between the signal amplitude and energy differs for α events compared to β/γ events due to pulse shape differences, which vary across detectors. Consequently, α energies, which were determined separately, are not reported in this work. As a result, the energy spectrum for all detectors and datasets shown in Figure 3 has many α peaks above 4 MeV electron-equivalent energy that are distributed incoherently when they are calibrated with the functions for β/γ events.

Events in the 2.7–3.6 MeV energy range were selected for the $0\nu\beta\beta$ study. The background energy distribution was approximated as a linear combination of flat and exponential background components. The exponential component includes high-energy $2\nu\beta\beta$ -decay events and β background from internal and surface contamination of the crystal [23]. The flat component is introduced to describe high energy γ s from neutron capture, external sources such as rock and radon in the air, and residual β and α events due to incomplete rejection.

Considering the background (b) and the $0\nu\beta\beta$ decay signal (s) can be expressed in terms of the decay rate ($\Gamma^{0\nu} = \ln 2/T_{1/2}^{0\nu}$), the number of ^{100}Mo nuclei (N_{100}), the detection efficiency (ε) for the $0\nu\beta\beta$ decay of ^{100}Mo (shown in Table I), and the DAQ livetime (t) as $s = \varepsilon \Gamma^{0\nu} N_{100} t$. An unbinned likelihood function was constructed as follows:

$$\mathcal{L} = \prod_{i=1}^N \prod_{j=1}^{n_i} \frac{(s_i + b_i)^{n_i} e^{-s_i - b_i}}{n_i!} \cdot f_i^{s+b}(E_j^i) \cdot \pi(\varepsilon_i, \nu_i), \quad (1)$$

where i and j are indices of the detector and its events,

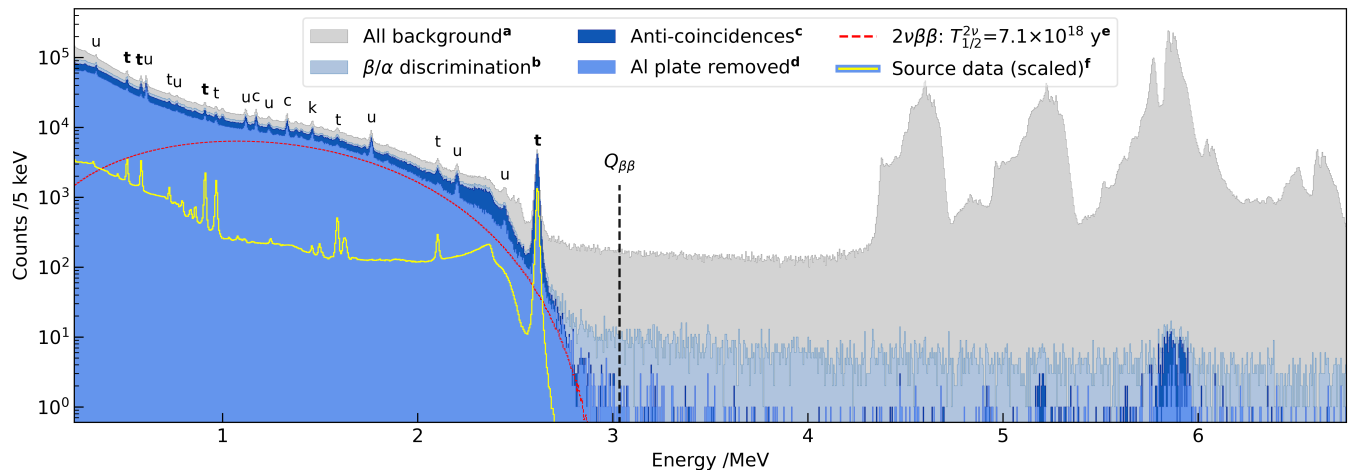


FIG. 3. Energy distributions of AMoRE-I data corresponding to 8.02 kg-year exposure, following step-by-step selections— **a**: raw data events after removing non-physical signals, **b**: β/γ events after selection using the pulse shape discrimination and L/H ratio, **c**: after all anti-coincidence selection, **d**: after removal of the aluminum plates, **e**: simulated two-neutrino double beta ($2\nu\beta\beta$) decay component corresponding to the exposure of **d** [36–38]. The source calibration spectrum (**f**, yellow line) is scaled to match the size of 2.615 MeV γ peak in **d**. Some background events remained in the high-energy range after all cuts, such as those in 5–6 MeVee, due to inefficient α rejection in the LMO data. Letters above prominent γ peaks denote the corresponding decay chains: u for uranium-238, t for thorium-232, c for cobalt-60, and k for potassium-40.

respectively, and n_i is the number of observed events at the i^{th} detector. The expected spectral shape was described by the probability density function, f^{s+b} , that includes a background model, with flat and exponential components, plus a signal peak in the form of a Bukin function for fully contained $0\nu\beta\beta$ events. Efficiency (ε_i) and peak shape parameters (ν_i) were treated as nuisance parameters with Gaussian priors (π).

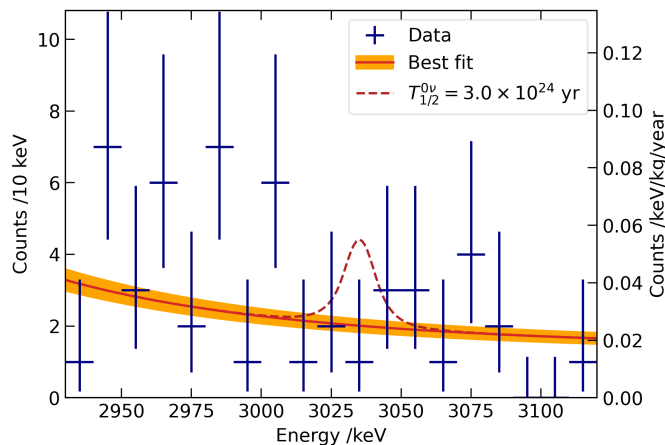


FIG. 4. The energy spectrum of selected events in the region of interest. The points with error bars are measured data with the 1σ Poisson confidence intervals. The solid blue curve is the best fit with a null signal, and the shaded region denotes the combined uncertainty of the fit. The dashed red curve shows the expected signal shape for a $0\nu\beta\beta$ decay half-life of 3.0×10^{24} years, the upper limit at a 90% confidence level from this study.

The minimized negative-log-likelihood was profiled over the sensitive range of $\Gamma^{0\nu}$ from 0 to $\sim 10^{-23}$ year $^{-1}$, and the best fit was found at $\Gamma^{0\nu} = 0.0$ year $^{-1}$, meaning that no event excess was found over the assumed background shape, as shown in Fig. 4. The corresponding limit on the half-life of the $0\nu\beta\beta$ decay of ^{100}Mo was evaluated at a 90% confidence level to be:

$$T_{1/2}^{0\nu} > 3.0 \times 10^{24} \text{ years}, \quad (2)$$

which extends the CUPID-Mo limit, 1.8×10^{24} years [19].

The posterior analysis leads to a total background level of $b = 0.025 \pm 0.002$ counts/keV/kg/year. Among the AMoRE-I detectors, LMO detectors showed a slightly lower background rate of 0.021 ± 0.005 counts/keV/kg/year on average, while background counting rate of the CMO detectors is 0.026 ± 0.003 counts/keV/kg/year. The total background rate in AMoRE-I was reduced by ~ 15 times compared to that of AMoRE-pilot.

We calculated the effective Majorana mass within the theoretical framework of the light neutrino exchange model, incorporating the phase space factor [39–41] and nuclear matrix elements (NMEs) [42–49]. The range of inferred upper limits on the effective Majorana mass is $m_{\beta\beta} < (210\text{--}350)$ meV assuming an axial vector coupling constant $g_A = 1.27$. If we include the first shell model calculation recently published for ^{100}Mo in [50], which presents the lowest NME among the theoretical values, the range of limits extends to $m_{\beta\beta} < (210\text{--}610)$ meV. The lower limit is derived from an energy density functional considering the nuclear deformation and pairing fluctuation [44], while the upper limit is based on a shell model

that explicitly includes the short-range correlations [50].

We are preparing AMoRE-II at Yemilab [51], at a depth of ~ 1000 meter (~ 2700 meter water equivalent) underground with a muon rate about a quarter of that at Y2L [52]. We have developed an LMO detector module with improved energy resolution and alpha background rejection [53, 54]. The radiopurity of all materials for AMoRE-II has been measured and evaluated for their contribution to background levels [55]. Over 300 LMO crystals have been grown, and a total of 360 crystals will be used in AMoRE-II. The background level for AMoRE-II is projected to be less than 1×10^{-4} counts/keV/kg/year based on radioassay data and GEANT4 simulations [56]. The discovery sensitivity is projected to be approximately 4.5×10^{26} years for five years of data collection.

We thank the Korea Hydro and Nuclear Power (KHNP) Company for providing underground laboratory space at Yangyang and the IBS Research Solution Center (RSC) for providing high-performance computing resources. This research is supported by Grant Nos. IBS-R016-D1 and IBS-R016-A2. It is also supported by the National Research Foundation of Korea (NRF-2021R1I1A3041453) and the National Research Facilities & Equipment Center (NFEC) of Korea (No. 2019R1A6C1010027). We appreciate the support by the Ministry of Science and Higher Education of the Russian Federation (N121031700314-5), the MEPHI Program Priority 2030. The group from the Institute for Nuclear Research (Kyiv, Ukraine) was supported in part by the program of the National Academy of Sciences of Ukraine, “Fundamental research on high-energy physics and nuclear physics (international cooperation).” These acknowledgements are not to be interpreted as an endorsement of any statement made by any of our institutes, funding agencies, governments, or their representatives.

* yoomin@ibs.re.kr

- [1] Y. Fukuda *et al.* (Super-Kamiokande), Evidence for oscillation of atmospheric neutrinos, *Phys. Rev. Lett.* **81**, 1562 (1998), arXiv:hep-ex/9807003.
- [2] Q. R. Ahmad *et al.* (SNO), Direct evidence for neutrino flavor transformation from neutral current interactions in the Sudbury Neutrino Observatory, *Phys. Rev. Lett.* **89**, 011301 (2002), arXiv:nucl-ex/0204008.
- [3] G. Bak *et al.* (RENO), Measurement of Reactor Antineutrino Oscillation Amplitude and Frequency at RENO, *Phys. Rev. Lett.* **121**, 201801 (2018), arXiv:1806.00248 [hep-ex].
- [4] D. Adey *et al.* (Daya Bay), Measurement of the Electron Antineutrino Oscillation with 1958 Days of Operation at Daya Bay, *Phys. Rev. Lett.* **121**, 241805 (2018), arXiv:1809.02261 [hep-ex].
- [5] M. A. Acero *et al.* (NOvA), Improved measurement of neutrino oscillation parameters by the NOvA experiment, *Phys. Rev. D* **106**, 032004 (2022), arXiv:2108.08219 [hep-ex].
- [6] K. Abe *et al.* (T2K), Measurements of neutrino oscillation parameters from the T2K experiment using 3.6×10^{21} protons on target, *Eur. Phys. J. C* **83**, 782 (2023), arXiv:2303.03222 [hep-ex].
- [7] M. Aker *et al.* (KATRIN), Direct neutrino-mass measurement with sub-electronvolt sensitivity, *Nature Phys.* **18**, 160 (2022), arXiv:2105.08533 [hep-ex].
- [8] N. Aghanim *et al.* (Planck), Planck 2018 results. VI. Cosmological parameters, *Astron. Astrophys.* **641**, A6 (2020), [Erratum: *Astron. Astrophys.* 652, C4 (2021)], arXiv:1807.06209 [astro-ph.CO].
- [9] R. N. Mohapatra and G. Senjanovic, Neutrino Mass and Spontaneous Parity Nonconservation, *Phys. Rev. Lett.* **44**, 912 (1980).
- [10] E. Majorana, Teoria simmetrica dell’elettrone e del positrone, *Nuovo Cim.* **14**, 171 (1937), <https://inspirehep.net/literature/8251>.
- [11] M. Agostini, G. Benato, J. A. Detwiler, J. Menéndez, and F. Vissani, Toward the discovery of matter creation with neutrinoless $\beta\beta$ decay, *Rev. Mod. Phys.* **95**, 025002 (2023), arXiv:2202.01787 [hep-ex].
- [12] J. Schechter and J. W. F. Valle, Neutrinoless Double beta Decay in SU(2) x U(1) Theories, *Phys. Rev. D* **25**, 2951 (1982).
- [13] M. Fukugita and T. Yanagida, Baryogenesis Without Grand Unification, *Phys. Lett. B* **174**, 45 (1986).
- [14] E. L. Fireman, A measurement of the half-life of double beta-decay from (50)Sn-124, *Phys. Rev.* **75**, 323 (1949).
- [15] S. Abe *et al.* (KamLAND-Zen), Search for the Majorana Nature of Neutrinos in the Inverted Mass Ordering Region with KamLAND-Zen, *Phys. Rev. Lett.* **130**, 051801 (2023), arXiv:2203.02139 [hep-ex].
- [16] A. Campani, New Results on $0\nu\beta\beta$ Decay from the CUORE Experiment, *LHEP* **2024**, 516 (2024).
- [17] M. Agostini *et al.* (GERDA), Final Results of GERDA on the Search for Neutrinoless Double- β Decay, *Phys. Rev. Lett.* **125**, 252502 (2020), arXiv:2009.06079 [nucl-ex].
- [18] E. Armengaud *et al.* (CUPID), New Limit for Neutrinoless Double-Beta Decay of ^{100}Mo from the CUPID-Mo Experiment, *Phys. Rev. Lett.* **126**, 181802 (2021), arXiv:2011.13243 [nucl-ex].
- [19] C. Augier *et al.*, Final results on the $0\nu\beta\beta$ decay half-life limit of ^{100}Mo from the CUPID-Mo experiment, *Eur. Phys. J. C* **82**, 1033 (2022), arXiv:2202.08716 [nucl-ex].
- [20] H. Bhang *et al.*, AMoRE experiment: a search for neutrinoless double beta decay of ^{100}Mo isotope with $^{40}\text{Ca}^{100}\text{MoO}_4$ cryogenic scintillation detector, *Topics in astroparticle and underground physics. Proceedings, 12th International Conference, TAUP 2011, Munich, Germany, September 5-9, 2011*, *J. Phys. Conf. Ser.* **375**, 042023 (2012).
- [21] V. Alenkov *et al.* (AMoRE), Technical Design Report for the AMoRE $0\nu\beta\beta$ Decay Search Experiment, (2015), arXiv:1512.05957 [physics.ins-det].
- [22] V. Alenkov *et al.* (AMoRE), First Results from the AMoRE-Pilot neutrinoless double beta decay experiment, *Eur. Phys. J.* **C79**, 791 (2019), arXiv:1903.09483 [hep-ex].
- [23] V. Alenkov *et al.* (AMoRE), Alpha backgrounds in the AMoRE-Pilot experiment, *Eur. Phys. J. C* **82**, 1140 (2022), arXiv:2107.07704 [physics.ins-det].

- [24] A. Agrawal *et al.* (AMoRE), Background study of the AMoRE-pilot experiment, *Astroparticle Physics* **162**, 102991 (2024), arXiv:2401.07476 [nucl-ex].
- [25] C. S. Kang, J. A. Jeon, H. S. Jo, G. B. Kim, H. L. Kim, I. Kim, S. R. Kim, Y. H. Kim, D. H. Kwon, C. Lee, H. J. Lee, M. K. Lee, S. H. Lee, S. Y. Oh, J. H. So, and Y. S. Yoon, MMC-based low-temperature detector system of the AMoRE-Pilot experiment, *Superconductor Science and Technology* **30**, 084011 (2017).
- [26] K. R. Woo, H. B. Kim, H. L. Kim, Y. H. Kim, D. H. Kwon, D. Y. Lee, H. J. Lee, S. H. Lee, Y. C. Lee, and H. S. Lim, An MMC-Based Temperature Control System for a Long-Term Data Collection, *J. Low Temp. Phys.* **209**, 1218 (2022).
- [27] C. Lee, H. S. Jo, C. S. Kang, G. B. Kim, I. Kim, Y. H. Kim, H. J. Lee, and J. H. So, Vibration Mitigation for a Cryogen-Free Dilution Refrigerator for the AMoRE-Pilot Experiment, *J. Low Temp. Phys.* **193**, 786 (2018).
- [28] M. B. Kim, J. S. Chung, J. A. Jeon, C. S. Kang, H. B. Kim, H. L. Kim, S. C. Kim, S. G. Kim, S. R. Kim, W. T. Kim, Y. H. Kim, D. H. Kwon, D. Y. Lee, H. J. Lee, M. K. Lee, S. H. Lee, Y. C. Lee, H. S. Lim, and K. R. Woo, Large Area Light Detectors With MMC Readouts, *IEEE Transactions on Applied Superconductivity* **33**, 1 (2023).
- [29] D. H. Kwon, J. A. Jeon, H. S. Jo, H. B. Kim, H. L. Kim, I. Kim, S. R. Kim, Y. H. Kim, H. Lee, M. K. Lee, *et al.*, Stabilization Heaters for Low-Temperature Thermal Calorimeters, *J. Low Temp. Phys.* **200**, 312 (2020).
- [30] H. B. Kim *et al.*, Status and Performance of the AMoRE-I Experiment on Neutrinoless Double Beta Decay, *J. Low Temp. Phys.* **209**, 962 (2022), arXiv:2211.02825 [physics.ins-det].
- [31] H. S. Lim, J. S. Chung, H. S. Jo, *et al.*, An analysis method of heat and light detection with scintillating crystals, *J. Low Temp. Phys.* (submitted).
- [32] G. B. Kim, J. H. Choi, H. S. Jo, *et al.*, Novel measurement method of heat and light detection for neutrinoless double beta decay, *Astroparticle Physics* **91**, 105 (2017).
- [33] RooBukinPdf Class Reference, <https://root.cern.ch/doc/master/classRooBukinPdf.html>.
- [34] B. Mailyan, B. Sharma, H. J. Kim, S. C. Kim, W. T. Kim, Y. D. Kim, Y. H. Kim, M. H. Lee, and K. R. Woo, Light Collection of Some Molybdate Crystal Absorbers for Cryogenic Calorimeters at Millikelvin Temperatures, *IEEE Trans. Nucl. Sci.* **70**, 1307 (2023).
- [35] K. R. Woo, J. S. Chung, D. H. Hwang, *et al.*, Thermal Model Improvement in Phonon Detection Channels Using a Scintillating Crystal, *J. Low Temp. Phys.* <https://doi.org/10.1007/s10909-024-03089-y> (2024).
- [36] S. Agostinelli *et al.* (GEANT4), GEANT4—a simulation toolkit, *Nucl. Instrum. Meth. A* **506**, 250 (2003).
- [37] O. A. Ponkratenko, V. I. Tretyak, and Y. G. Zdesenko, The Event generator DECAY4 for simulation of double beta processes and decay of radioactive nuclei, *Phys. Atom. Nucl.* **63**, 1282 (2000), arXiv:nucl-ex/0104018.
- [38] C. Augier *et al.* (CUPID-Mo), Measurement of the $2\nu\beta\beta$ Decay Rate and Spectral Shape of Mo100 from the CUPID-Mo Experiment, *Phys. Rev. Lett.* **131**, 162501 (2023), arXiv:2307.14086 [nucl-ex].
- [39] J. Kotila and F. Iachello, Phase space factors for double- β decay, *Phys. Rev. C* **85**, 034316 (2012), arXiv:1209.5722 [nucl-th].
- [40] M. Mirea, T. Pahomi, and S. Stoica, Values of the phase space factors involved in double beta decay, *Rom. Rep. Phys.* **67**, 872 (2015).
- [41] S. Stoica and M. Mirea, Phase Space Factors for Double-Beta Decays, *Front. in Phys.* **7**, 12 (2019).
- [42] P. K. Rath, R. Chandra, K. Chaturvedi, P. Lohani, P. K. Raina, and J. G. Hirsch, Neutrinoless $\beta\beta$ decay transition matrix elements within mechanisms involving light Majorana neutrinos, classical Majorons, and sterile neutrinos, *Phys. Rev. C* **88**, 064322 (2013), arXiv:1308.0460 [nucl-th].
- [43] F. Šimkovic, V. Rodin, A. Faessler, and P. Vogel, $0\nu\beta\beta$ and $2\nu\beta\beta$ nuclear matrix elements, quasiparticle random-phase approximation, and isospin symmetry restoration, *Phys. Rev. C* **87**, 045501 (2013), arXiv:1302.1509 [nucl-th].
- [44] N. López Vaquero, T. R. Rodríguez, and J. L. Egido, Shape and pairing fluctuations effects on neutrinoless double beta decay nuclear matrix elements, *Phys. Rev. Lett.* **111**, 142501 (2013), arXiv:1401.0650 [nucl-th].
- [45] J. Barea, J. Kotila, and F. Iachello, $0\nu\beta\beta$ and $2\nu\beta\beta$ nuclear matrix elements in the interacting boson model with isospin restoration, *Phys. Rev. C* **91**, 034304 (2015), arXiv:1506.08530 [nucl-th].
- [46] J. Hyvärinen and J. Suhonen, Nuclear matrix elements for $0\nu\beta\beta$ decays with light or heavy Majorana-neutrino exchange, *Phys. Rev. C* **91**, 024613 (2015).
- [47] L. S. Song, J. M. Yao, P. Ring, and J. Meng, Nuclear matrix element of neutrinoless double- β decay: Relativity and short-range correlations, *Phys. Rev. C* **95**, 024305 (2017), arXiv:1702.02448 [nucl-th].
- [48] F. Šimkovic, A. Smetana, and P. Vogel, $0\nu\beta\beta$ nuclear matrix elements, neutrino potentials and SU(4) symmetry, *Phys. Rev. C* **98**, 064325 (2018), arXiv:1808.05016 [nucl-th].
- [49] P. K. Rath, R. Chandra, K. Chaturvedi, and P. K. Raina, Nuclear Transition Matrix Elements for Double- β Decay Within PHFB Model, *Front. in Phys.* **7**, 64 (2019).
- [50] L. Coraggio, N. Itaco, G. De Gregorio, A. Gargano, R. Mancino, and F. Nowacki, Shell-model calculation of ^{100}Mo double- β decay, *Phys. Rev. C* **105**, 034312 (2022), arXiv:2203.01013 [nucl-th].
- [51] K. S. Park, Y. D. Kim, K. M. Bang, H. K. Park, M. H. Lee, J. So, S. H. Kim, J. H. Jang, J. H. Kim, and S. B. Kim, Construction of Yemilab, *Front. in Phys.* **12**, 1323991 (2024), arXiv:2402.13708 [astro-ph.IM].
- [52] H. Prihtiadi (COSINE-100), Muon detector and muon flux measurement at Yangyang Underground Laboratory for the COSINE-100 Experiment, *PoS ICRC2017*, 883 (2018).
- [53] W. T. Kim *et al.*, Optimization of cryogenic calorimetric detection with lithium molybdate crystals for AMoRE-II experiments, *JINST* **17** (07), P07034.
- [54] W. T. Kim *et al.*, Test Measurements of an MMC-Based 516-g Lithium Molybdate Crystal Detector for the AMoRE-II Experiment, *J. Low Temp. Phys.* **209**, 299 (2022).
- [55] A. Agrawal *et al.* (AMoRE), Radioassay of the materials for AMoRE-II experiment, *Front. in Phys.* **12**, 1362209 (2024).
- [56] A. Agrawal *et al.* (AMoRE), Projected background and sensitivity of AMoRE-II, In preparation (2024).